Supplementary Information

Alternative ground states enable pathway switching in biological electron transfer

Electrochemical determinations

Au working electrodes were coated with a mixed self-assembled monolayer by overnight incubation in an ethanolic 2mM HS-$(CH_2)_{15}$-CH_3 / 3mM HSs-$(CH_2)_{16}$-OH solution. After thorough rinsing with ethanol and deionized water, the coated electrodes were incubated in a 100 μM protein solution (in 10 mM acetate buffer, pH 4.6) during 2 hours for protein adsorption and then transferred to the electrochemical cell. Measurements were performed in a 10 mM acetate buffer/200mM KNO_3 buffer. The temperature was held fixed during measurements by controlling the temperature of a water jacket cell coupled to a circulating thermostat.

X-Ray Absorption Spectroscopy

The beam line was configured with a Si[220] monochromator and a Rh-coated mirror upstream of the monochromator set to the 13 KeV energy cutoff to reject harmonics. A second Rh mirror downstream of the monochromator was used to focus the beam. Data were collected in fluorescence mode using a high-count-rate Canberra 30-element Ge array detector with maximum count rates below 120 kHz. A 6μ Z-1 Ni oxide filter and Soller slit assembly were placed in front of the detector to reduce the elastic scatter peak. Energy calibration was achieved by reference to the first inflection point of a copper foil (8980.3 eV) placed between the second and third ionization chamber. To avoid photoreduction, each scan was measured as a separate spot (1mm ×2 mm) on the sample. Two scans were collected for each sample and averaged.

The samples (80 μL) were measured as aqueous glasses (>20% ethylene glycol) at 10-15 K. Six scans of a sample containing only sample buffer were collected, averaged and subtracted from the averaged data for the protein samples to

remove Z-1 K_β fluorescence and produce a flat pre-edge baseline. Data reduction and background subtraction were performed using the program modules of EXAFSPAK (1). Data from each detector channel were inspected for glitches, drops-outs, or other non-linear behaviour before inclusion in the final average. EXAFS spectra were simulated using EXCURVE 9.2 as described previously (2, 3).

Computational methods.

For the Cu_A site, the coordinating histidines were simulated in the HIE tautomeric state (i.e with proton in the epsilon nitrogen). In the case of the M160H mutant, two different species were studied (coordinating either through N^{ε} or $N^{\delta)}$, since there is no experimental evidence that allows to properly assign the tautomeric state of the H160 ligand. All simulations were performed at 1 atm. and the desired temperature (production simulations were performed at 300K) were maintained with the Berendsen barostat and thermostat, respectively. Periodic boundary conditions and Ewald sums (grid spacing of 1 Å) were used to treat long-range electrostatic interactions; a 12 Å cut-off was used for computing direct interactions. The SHAKE algorithm was used to keep bonds involving hydrogen atoms at their equilibrium length. All simulations were performed with the PMEMD module of the AMBER11 package(4). The Amber ff99SB force field was used for all residues but the Cu_A site, whose parameters were developed and thoroughly tested for the present work using standard procedures(5). Partial atomic charges for the copper ion and the coordination sphere ligands were determined using the RESP procedure(6), using the optimized *in vacuum* structure of the corresponding site computed at the DFT level as described below.

For each species we ran an equilibration process which consisted of an energy minimization of the initial structures (2000 steps of conjugate gradient), followed by a slow heating from 0K (during 200ps) up to the desired temperature of 300K. Starting from these equilibrated structures 10 ns long production MD simulations in explicit water were performed. After analysis of the MD simulations, selected snapshots of each system were slowly cooled to 0 K (during 200 ps) in order to obtain the initial structures for the QM/MM simulations.

QM/MM calculations were performed at the DFT level using the SIESTA (7) code with the QM/MM implementation called *Hybrid* (8). For all atoms, basis sets of double zeta plus polarization quality were employed with cut-off and energy shift

values of 150 Ry and 25 meV. All calculations were performed using the generalized gradient approximation functional proposed by Perdew, Burke, and Ernzerhof (PBE)(9). The interface between the QM and MM portions of the system was treated with the scaled position link atom method. For all systems the spin-unrestricted approximation was used, unless otherwise stated.

Simulations were performed for both the oxidized (doublet) and reduced (singlet) states for all species. The QM subsystem included both copper atoms, the imidazole rings from the histidines, the S, C^{β} and corresponding H atoms from the cysteines, the complete amino acids which participate in the amide bond that provides the carbonyl ligand and the side chain of the corresponding ligand at the 160 position. The rest of the protein and water molecules were treated classically using the Amber force field. All atoms included in the MD simulation were included in the QM/MM system. Starting from the MD frozen (0 K) structure mentioned above, the $TtCu_A$ and mutants were optimized at the QM/MM level.

QM calculations were performed using Gaussian09 (10). The QM/MM optimized structures were used as a starting point for QM calculations. The His ligands were replaced by imidazole rings, the cysteines by $S\text{-}CH_3$ moiety and the Met and Gln axial ligands by $CH_3\text{-}S\text{-}CH_3$ and $CH_3\text{-}CO.NH\text{-}CH_3$ respectively. The mixed triple-zeta/double zeta (TZVP) basis set was used for Cu and S atoms, while the 6-31G* basis set were used on all the other atoms. Tight SCF convergence criteria were used for all calculations, while the geometry optimizations were performed without geometrical constraints. UVVis spectra were simulated performing time dependent DFT (TD-DFT) calculations, obtaining the energies and intensities of the 100 lowest energy electronic transitions. Relaxed PES scans of different scanning variables were performed: the Cu-Cu internuclear distance, the N-Cu-Cu-N dihedral angle formed between the two coordinating histidines, and the Cu_2S_2 plane which was variated as the S-Cu-S-Cu dihedral angle. The analysis of the MO compositions and the covalent contributions to chemical bonding were done using the Chemissian software package.

Estimation of the donor-acceptor electronic coupling matrix element H_{AB} was performed using the Pathways (11) plugin for VMD. Calculations were performed on the three available structures for the cytochrome c_{552}-Cu_A subunit complex structures from PDB ID 2FWL (12), and for the cytochrome *c* oxidase PDB ID 1XME (13). All these structures correspond to *Thermus thermophilus* proteins.

Nuclear Magnetic Resonance Spectroscopy

^{1}H-detected spectra were acquired with a triple-resonance (TXI) probehead using presaturation, PASE and SuperWEFT schemes on spectral windows of 48 – 360 kHz (total recycle times around 200 and 40 ms respectively). ^{1}H,^{13}C- and ^{1}H,^{15}N-HMQC experiments were acquired with 64-128 points in the indirect dimension setting the delay for coherence transfer close to the T_2 of the fastest relaxing ^{1}H signal for which a correlation was expected. Saturation Transfer Difference (STD) and NOE experiments on the broad signals from Cys'β protons were performed on samples prepared in 100% D_2O buffer, either completely oxidized for NOE experiments or partially reduced for STD experiments (*ca*. 10% reduced protein, obtained by addition of sodium ascorbate). Signals were irradiated for *ca*. 50 ms at a power of *ca*. 5 mW.

Carbon-13 detected spectra were acquired with a broad-band observe (BBO) using an excitation pulse of 6.9 μs at 88.67 W. Inverse gated decoupling was applied during acquisition of ^{13}C spectra. The carrier frequency was set to 800, 300, or -500 ppm depending on which signals were being studied at the moment. Total recycle times were around 35 ms for the observation of signals around 800 and -500 ppm, and *ca*. 300 ms for those near the diamagnetic region. STD experiments on ^{13}C signals were performed on samples containing *ca*. 10% reduced protein obtained by addition of sodium ascorbate. STD spectra were acquired with irradiation for *ca*. 40 ms at a power of *ca*. 0.1 - 5 mW. Assignments are described in detail in the supporting text, Figures S2 and S3, and Table S2.

The full assignment of ^{1}H, ^{13}C and ^{15}N resonances for the wild type protein has been recently reported by us, and the ^{1}H NMR spectrum of M160Q was already available. Here we have assigned the remaining ligand resonances in this mutant and all signals in M160H by a combination of 1D and 2D NOESY experiments, fast pulsing ^{1}H,^{13}C and ^{1}H,^{15}N HMQC spectra, and saturation transfer experiments. All the obtained assignments are given in Table S2. Analyses of the chemical shifts and their temperature dependences were performed as described previously(14).

The assignment of paramagnetically shifted signals in the M160H mutant revealed interesting facts. First, in contrast to the case of the M160Q mutant where only one His residue is affected by the substitution, the M160H substitution results in both native histidines being affected. Hence, in the M160H mutant, the chemical

shifts of both His114 and His157 reveal low spin densities on these nuclei compared to the wild type protein. The $^{1}H,^{15}N$-HMQC spectrum reveals the correlation between His157Hε2 and its ^{15}N nucleus (only observed at pH ≤ 5 and T ≤ 288 K, as in the wild type protein) and between His114Hε2 and its ^{15}N. However, an additional crosspeak is observed between a ^{15}N signal at 217 ppmand ^{1}H signal n^{*} at 10.5 ppm, absent both in wild type and in M160Q (Figure S3, pattern in cyan). The latter signal presents NOEs with two other ^{1}H signals, one of which is clearly shifted by paramagnetism. This spin system can thus be assigned to nuclei from the imidazole ring of His160. This result not only confirms the conclusion from EXAFS data, showing that the engineered ligand His160 effectively binds the copper ion, but also discloses the presence of unpaired electron spin density on its imidazole ring.

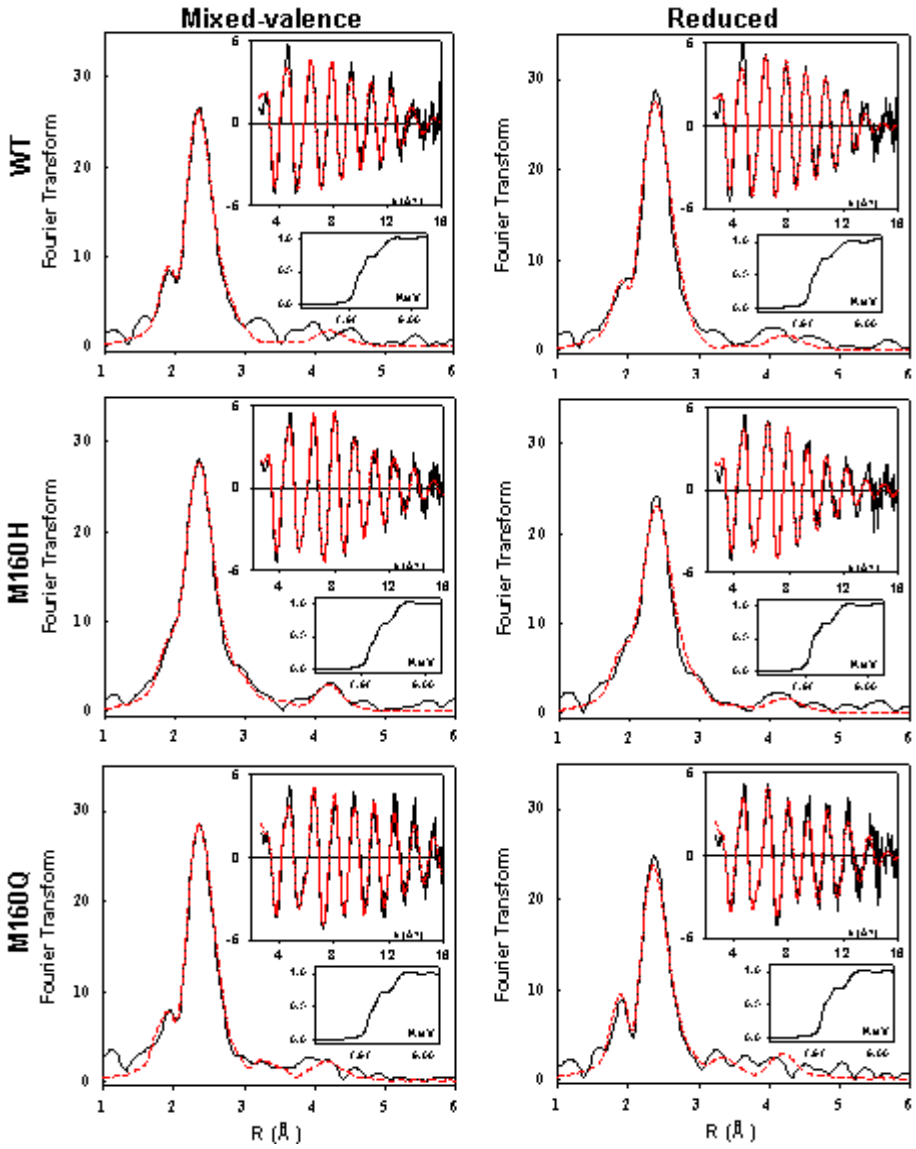

Figure S1. EXAFS data (black) and fits as detailed in table S1 (red)

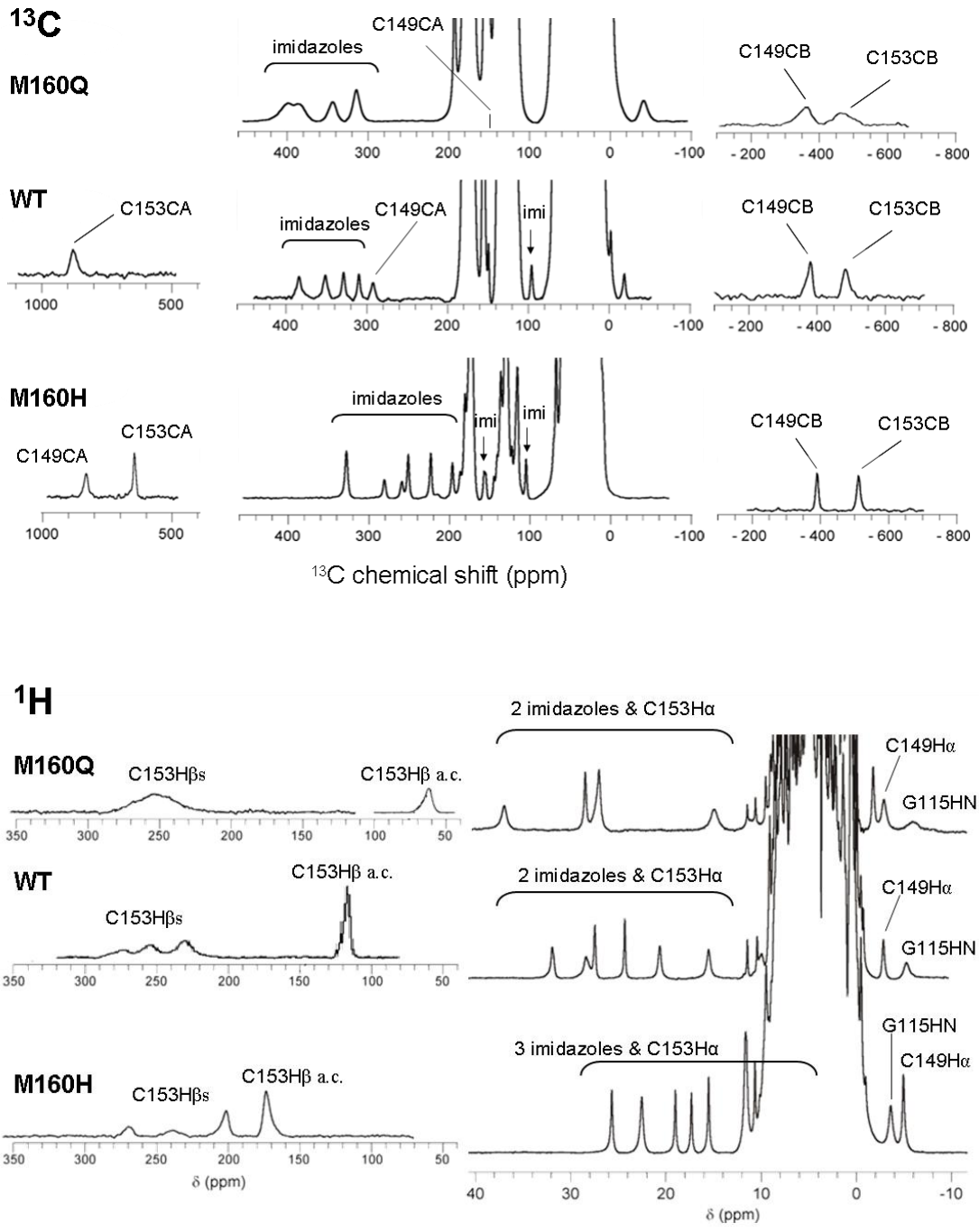

Figure S2. ^{1}H and ^{13}C NMR spectra of wild type CuA and the M160H and M160Q mutants, with the most important assignments in labels. The full assignment is reported in Table S2.

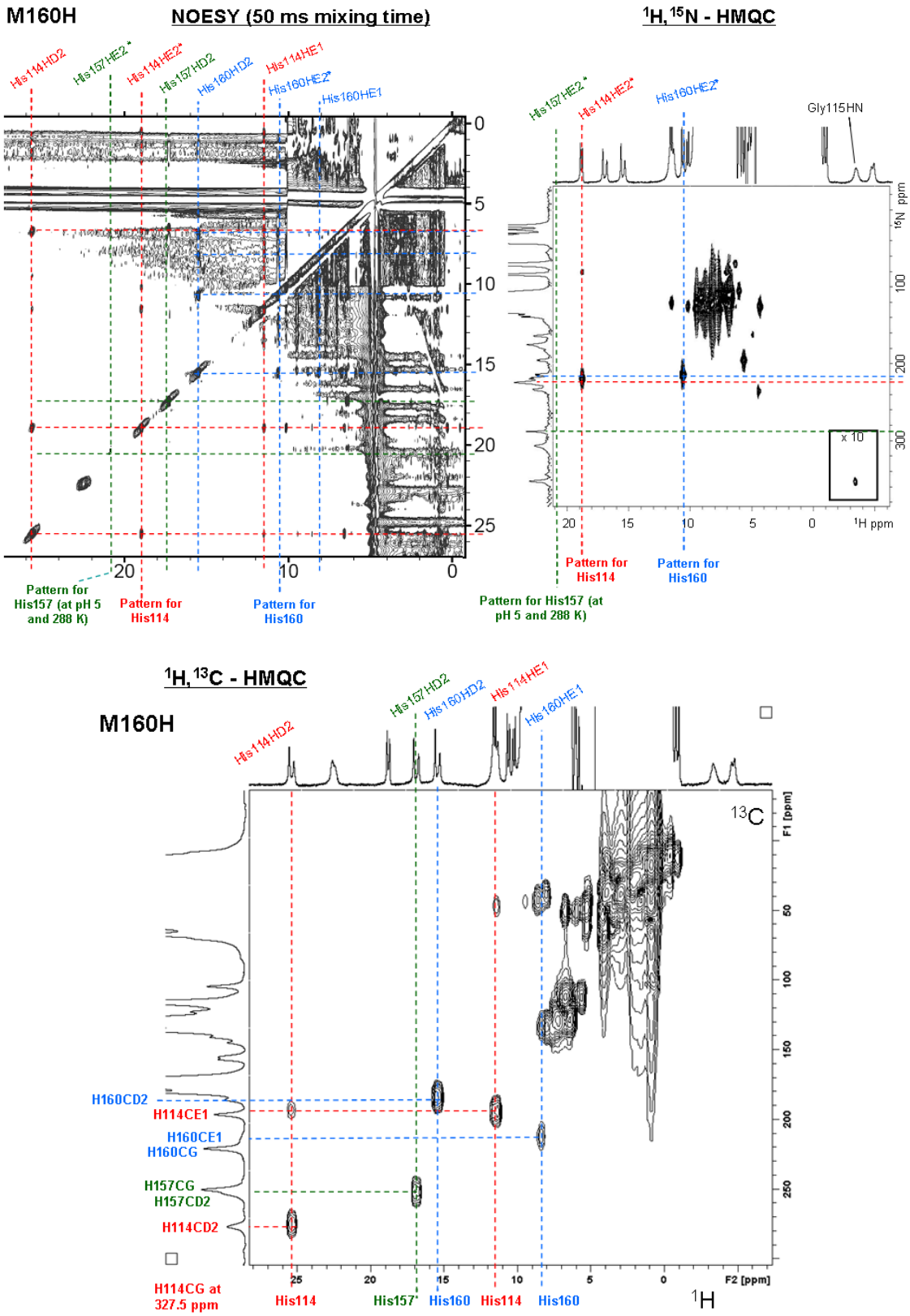

Figure S3. NMR spectra showing patterns for three His residues under paramagnetic effect in the M160H mutant.

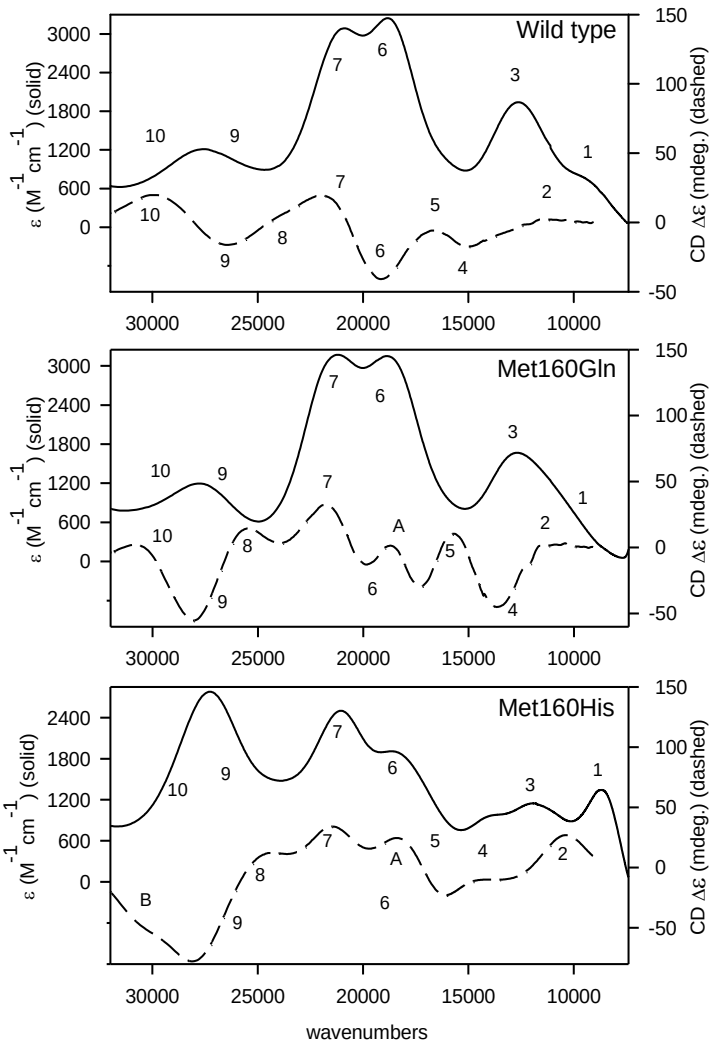

Figure S4. Absorption and CD spectra with full band numbering. Band assignments are given in Table S3.

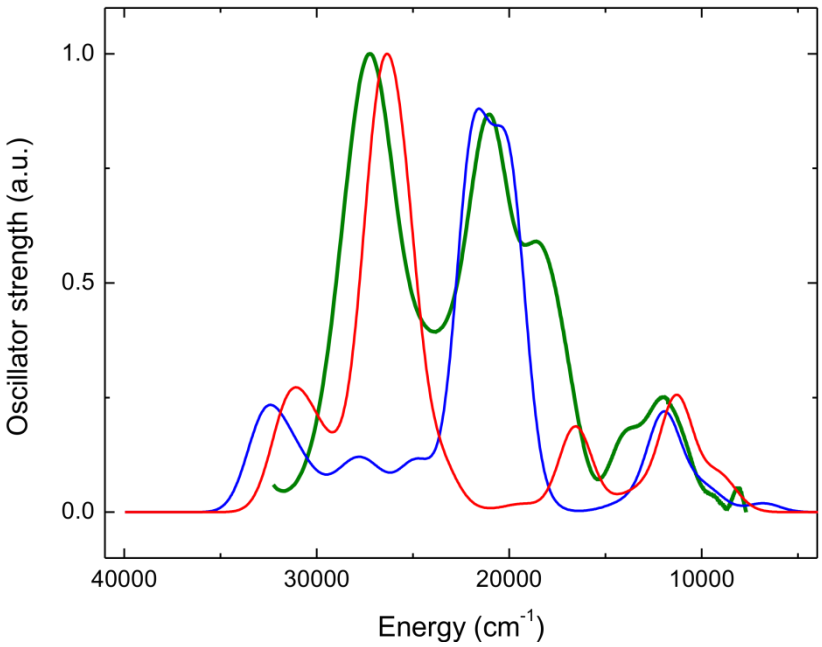

Figure S5. Experimental UV/Vis spectrum of M160H (green) at room temperature and TD-DFT calculations of UV/Vis spectra for both M160H σ_u^* (blue) and M160H π_u (red).

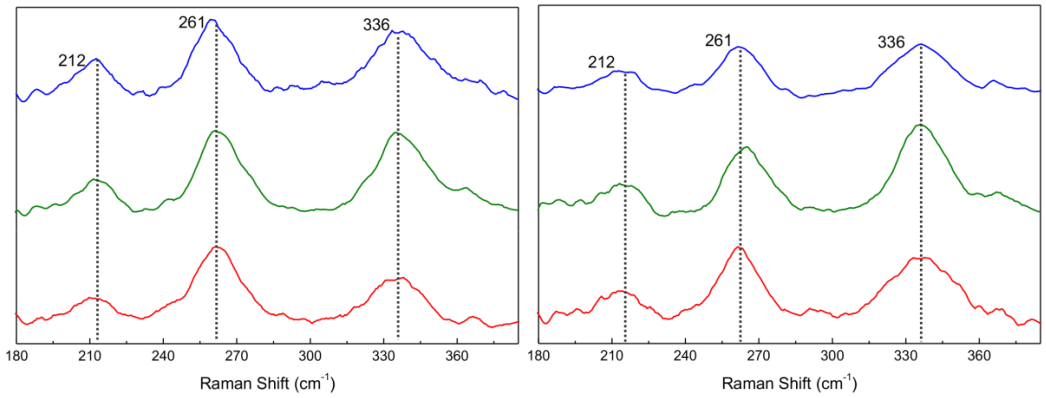

Figure S6. RR spectra of WT (blue), M160Q (green) and M160H (red) recorded at room temperature and pH 3.1 (left) and pH 6.1 (right).

.

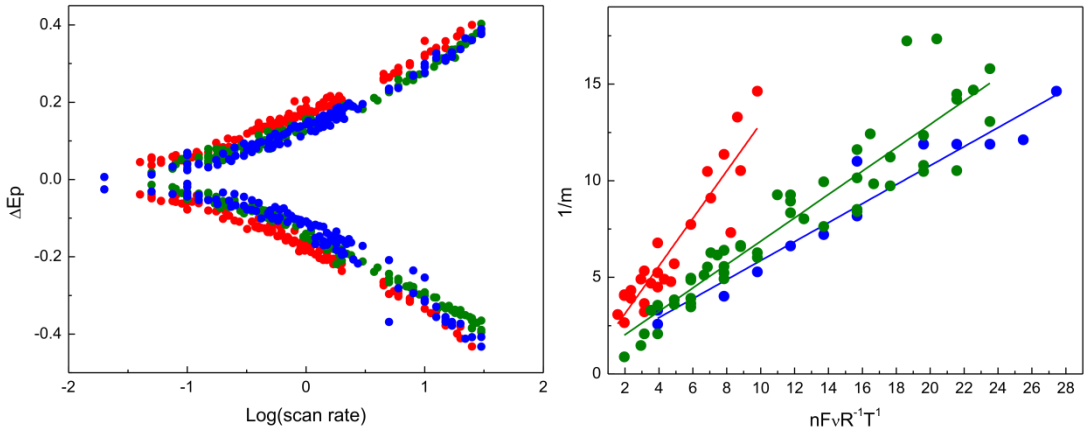

Figure S7. Left: trumpet plots of the difference in peak potential vs. log(scan rate) for WT (blue), M160Q (green) and M160H (red) obtained at 298 K. Reorganization energy values were obtained fitting the peak separations at constant temperature to the Marcus-DoS model. λ values (WT: 0.45 eV, M160Q: 0.45 eV, M160H: 0.7 eV) are in excellent agreement with those obtained from the Arrhenius plots (Figure S8). Right: Laviron's working curves obtained for determining k_{ET} values for WT (blue; 2.03 s^{-1}), M160Q (green; 1.65 s^{-1}) and M160H (red; 0.82 s^{-1}).

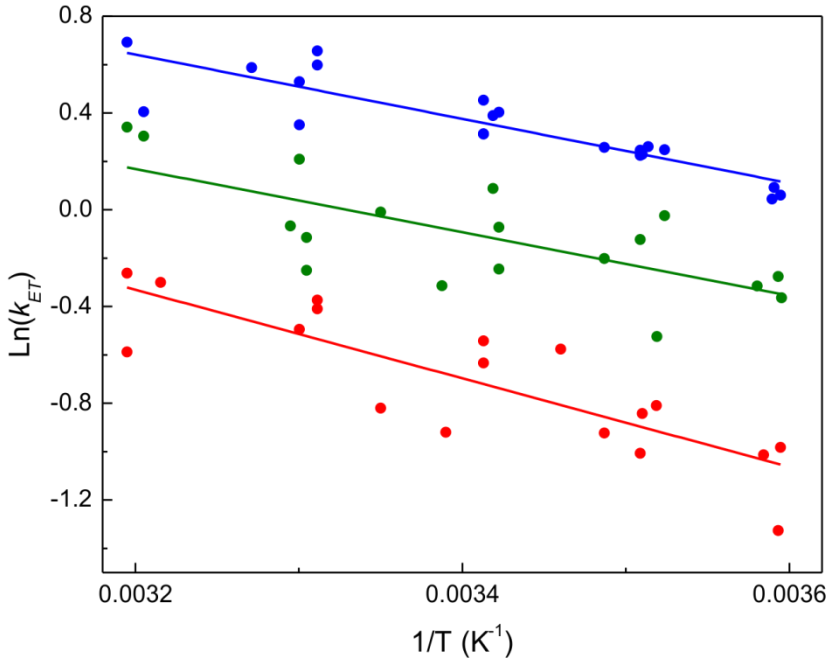

Figure S8. Arrhenius plots for the ET reaction rate. The reorganization energy values obtained are 0.46eV for WT (blue), 0.45eV for M160Q (green) and 0.63eV for M160H (red). These values are in excellent agreement with those obtained at constant temperature from the Marcus-DoS model.

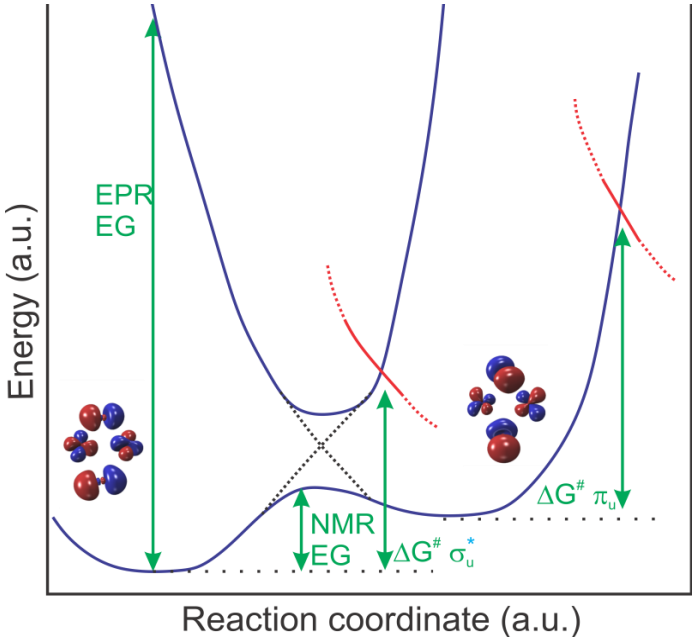

Figure S9. Model of the idealized potential energy surface for M160H. The curves for the oxidized and reduced state are shown in blue and red, respectively. The ET reaction could, in principle, take place at both crossings between the surfaces of different redox states. One of them is associated with the ET reaction in the σ_u^* GS, with a low $\Delta G^{\#}$, while the other one is corresponds to the ET reaction in the π_u state. The M160H mutant presents a unique feature: the magnitude of the energy gap (EG) between both GSs is smaller than $\Delta G^{\#}$ for the ET reaction in the σ_u^* GS. It is not known which is the reaction coordinate (RC) for the ET reaction (RC_{ET}), but we have shown that there are many RCs that yield a π_u GS (RC_{GS}) (see figures 1B, S10 and S11) . If both the RC_{ET} and the RC_{GS} are coupled, the ET reaction from the σ_u^* GS cannot occur: as the system begins its displacement towards the crossing point with the reduced σ_u^* GS parabola, the large (adiabatic) coupling between both GS in the oxidized state prevents this from happening. Instead, the system, now in the π_u state, continues to scan the RC, until the crossing point for the ET reaction in this GS state is reached. Thus, the observable parameters of the ET reaction for this mutant correspond to the π_u state.

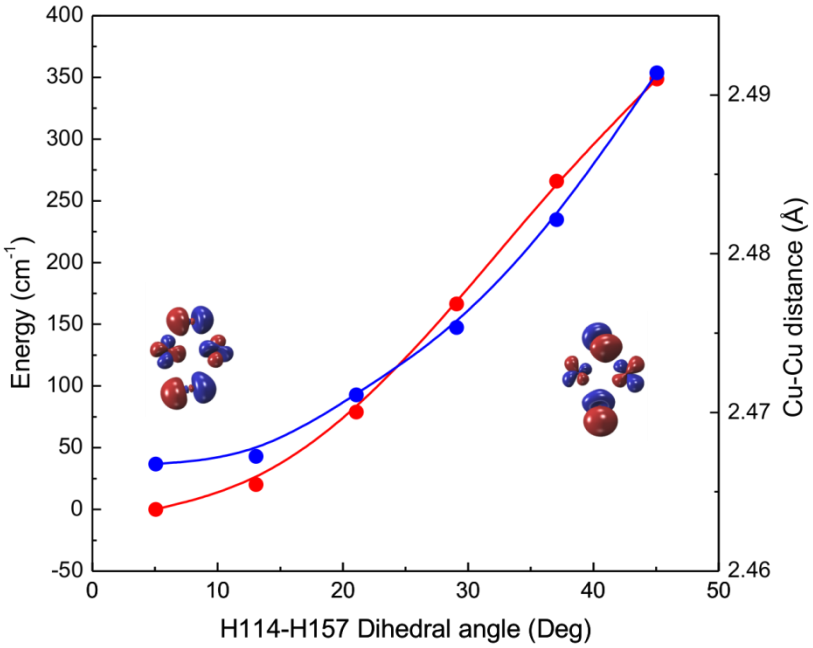

Figure S10. Energy (red) and Cu-Cu distance (blue) vs. the H114-H157 dihedral angle. At a 5º angle the GS HOMO has a σ_u^* symmetry, while at 30º the GS is a π_u. The Cu-Cu distance is slightly increased along the coordinate.

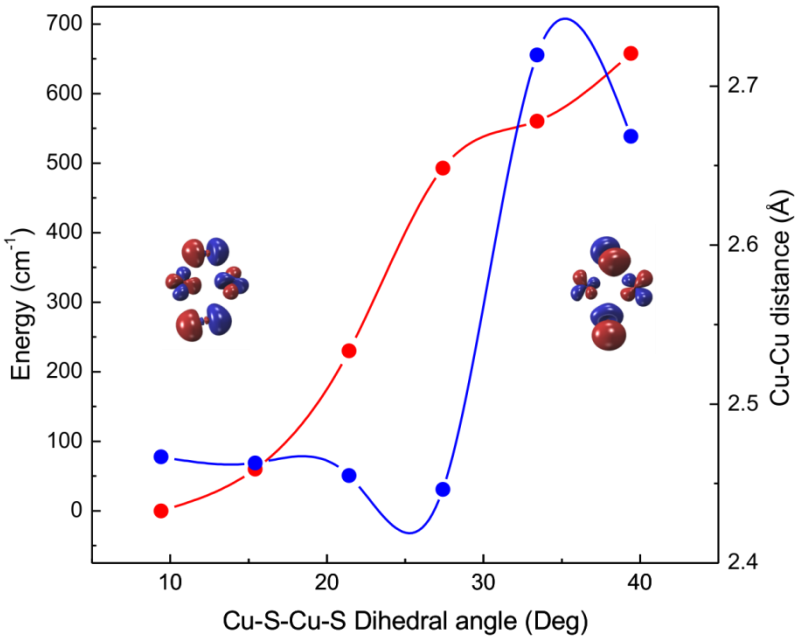

Figure S11. Energy (red) and Cu-Cu distance (blue) as a function of Cu-S-Cu-S dihedral angle. The calculations show that the equilibrium dihedral angles for the σ_u^* and π_u ground states are 10° and 35°, respectively. Note that for both ground states the Cu-Cu distance shortens slightly along the coordinate (dihedral angle), but it increases sharply at the point where the $\sigma_u^* \rightarrow \pi_u$ transition occurs.

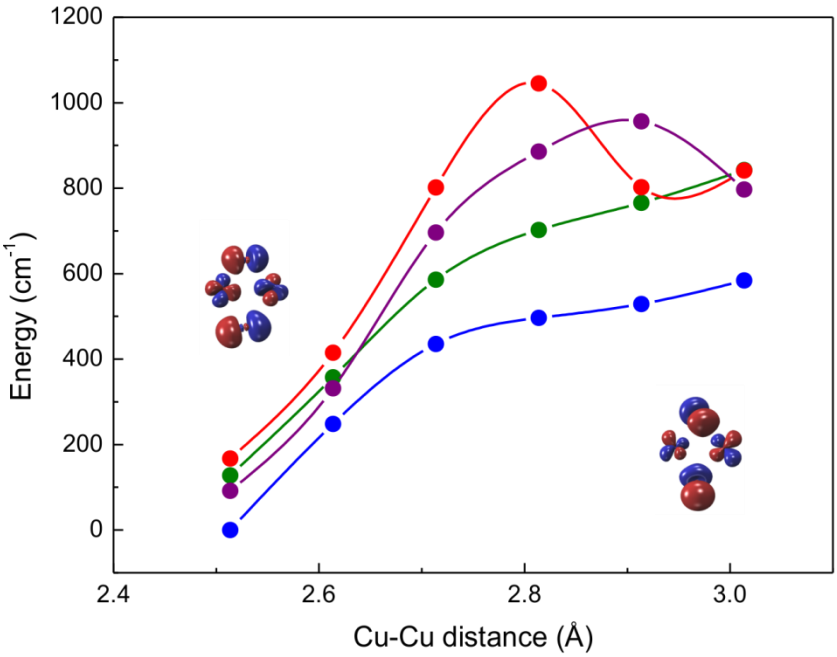

Figure S12. Effect of biologically relevant electric fields (EF) on the potential energy surface of Cu_A along the Cu-Cu distance coordinate. Blue: No EF applied. Green: EF applied on the S_{Cys}- S_{Cys}direction. Purple: EF applied on the Cu-Cu direction. Red: EF applied perpendicular to the Cu_2S_2 core. In all cases the EF strength is 10^9 V.m^{-1}.
The calculations predict that at around 2.5Å the GS HOMO has σ_u^* symmetry, while at 2.8 Å the GS is π_u. Note that the applied EF may affect both thermodynamics and kinetics of the transition, as revealed by the shapes of the different curves. In addition, it is observed that the EF may shift the equilibrium length for the π_u state. The magnitude of the effects depends on the direction of the applied field.

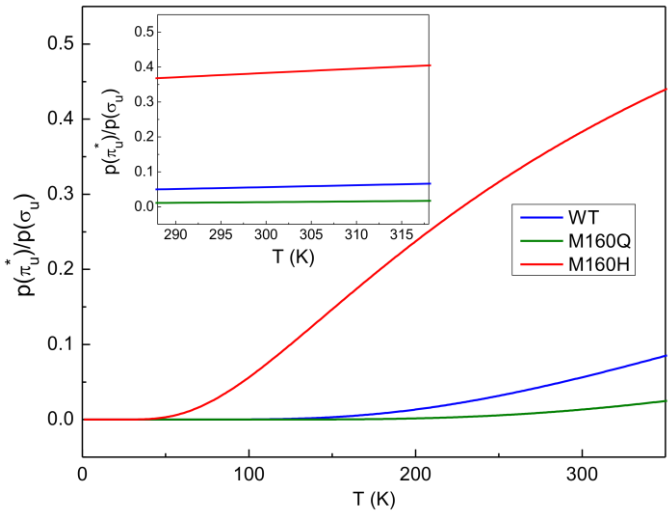

Figure S13. Population of the π_u ground state in Cu_A WT (blue), M160Q (green) and M160H (red) from 0K to 350K. Inset: Population of the π_u ground state in the temperature range of electrochemical determinations, where it remains practically constant.

Table S1. Fits obtained to the Cu K-EXAFS of WT and M160 variants of *T. thermophilus*cytochrome oxidase ba_3 by curve-fitting using the program EXCURVE 9.2.

	F[a]	No[b]	R (Å)[c]	DW (Å^2)	No[b]	R (Å)[c]	DW (Å^2)	No[b]	R (Å)[c]	DW (Å^2)	E_0
		Cu-N			Cu-S			Cu-Cu			
WT mixed-valence	0.393	1 His[d]	1.978	0.006	2	2.303	0.013	1	2.472	0.012	-2.17
					0.5	2.94	0.018				
WT reduced	0.369	1 His[d]	1.983	0.008	2	2.306	0.014	1	2.495	0.010	-1.85
					0.5	2.92	0.016				
M160H mixed-valence	0.191	1 His[d]	1.965	0.010	2	2.269	0.015	1	2.446	0.009	0.003
		0.5 O/N	2.63	0.010							
M160H reduced	0.374	1 His[d]	1.959	0.010	2	2.274	0.019	1	2.477	0.010	0.196
		0.5 O/N	2.61	0.009							
M160Q mixed-valence	0.360	1 His[d]	1.946	0.010	2	2.286	0.022	1	2.429	0.006	0.311
		0.5 O/N	2.54	0.013							
M160Q reduced	0.558	1 His[d]	1.943	0.005	2	2.295	0.021	1	2.443	0.010	0.517
		0.5 O/N	2.51	0.017							

[a] F is a least-squares fitting parameter defined as $F^2 = \frac{1}{N}\sum_{i=1}^{N} k^6 (Data - Model)^2$

[b] Coordination numbers are generally considered accurate to ± 25%

[c] In any one fit, the statistical error in bond-lengths is ±0.005 Å. However, when errors due to imperfect background subtraction, phase-shift calculations, and noise in the data are compounded, the actual error is probably closer to ±0.02 Å.

[d] Fits included both single and multiple scattering contributions from the imidazole ring

Table S2. Assignments of ^{1}H, ^{13}C and ^{15}N resonances under paramagnetic effect in wild type CuA and the M160H and M160Q mutants.

Residue / Nucleus	Wild type		M160H		M160Q	
	δ_{obs} (ppm)	$(A/h)_{app}$ (MHz)	δ_{obs} (ppm)	$(A/h)_{app}$ (MHz)	δ_{obs} (ppm)	$(A/h)_{app}$ (MHz)
Cys149						
Cβ	-379.4	-3.67	-392.1	-3.89	-358.7	-3.58
Cα	294.6	2.12	830.3	7.14	153.3	0.88
Hβ	262	9.37	195.2	7.21	308.0	11.38
Hβ	237	8.48	153.5	5.65	262.0	9.67
Hα	-2.9	-0.22	-3.5	-0.25	-2.9	-0.23
CO	151.7	-0.21	ND	ND	ND	ND
Cys153						
Cβ	-475.3	-4.56	-514	-5.04	-462.8	-4.57
Cα	880.5	7.43	646.5	5.47	ND	ND
Hβ	283	10.15	239.4	8.87	ND	ND
Hβ	117	4.21	242.7	8.99	61.0	2.26
Hα	27.55	0.92	22.6	0.76	11.0	0.34
CO	142	-0.28	ND	ND	ND	ND
His114						
Cε1	33.9	-0.92	196	0.56	ND	ND
Cδ2	353.6	2.11	280.3	1.49	398.9	2.58
Cγ	312.2	1.60	327.5	1.82	343.3	1.96
Hδ2	31.6	0.91	25.8	0.72	36.9	1.13
Hε2	24.2	0.46	19.1	0.29	28.4	0.64
Hε1	20.7	0.57	11.7	0.26	26.9	0.82
Nε2	239.7	2.69	220.5	0.21	ND	ND
Gly115						
HN	-5.2	-0.53	-3.5	-0.48	-6.0	-0.57
N	333.7	0.83	360	0.92	ND	ND
His157						
Cε1	98.4	-0.36	ND	ND	ND	ND
Cδ2	386.2	2.41	258.6	1.30	386.9	2.49
Cγ	331.2	1.77	250.8	1.07	314.9	1.67
Hδ2	27.46	0.74	17.4	0.39	27	0.75
Hε2	23.2	0.49	20.1	0.40	23.2	0.51
Hε1	15.5	0.37	ND	ND	14.9	0.36
Nε2	327.1	0.60	305	0.52	ND	ND
His160						
Cε1			ND	ND		
Cδ2			186.2	0.61		
Cγ			222.8	0.84		
Hδ2			15.6	0.32		
Hε2			10.5	0.03		
Hε1			8	0.00		
Nε2			217	0.13		

Table S3. Deconvolution of electronic absorption spectra, which gives rise to the band numbering in Figure S4.

	M160Q		WT		M160H	
	υ (cm^{-1})	**ε ($M^{-1}cm^{-1}$)**	**υ (cm^{-1})**	**ε ($M^{-1}cm^{-1}$)**	**υ (cm^{-1})**	**ε ($M^{-1}cm^{-1}$)**
10	28100	800	28000	800	27900	1500
9	26000	500	25800	500	26500	1500
8	23200	300	23400	650	23800	1000
7	21500	2850	21270	2600	21150	2340
6	18550	2900	18700	3100	18300	1660
5	15900	450	16050	645	16560	530
4	--	--	--	--	14500	600
3	12750	1650	12650	1960	12100	1100
2	--	--	--	--	10190	300
1	10250	550	9400	610	8600	1233

Table S4. Resonance Raman shifts obtained with excitation at 514.5 nm.

Symmetry	Raman Shift (cm^{-1})	Description
	212 WT	
B_u	212 M160Q	ν(Cu-N) + ν(Cu-S)
	212 M160H	
	262 WT	
A_g	264 M160Q	ν(Cu-S) + ν(Cu-N)
	262 M160H	
	336 WT	
A_g	336 M160Q	ν(Cu-S)
	336 M160H	

At this wavelength the RR spectra produced present enhancement of the Cu-S stretching modes for the σ_u^* symmetry. The π_u presents no absorption band at the excitation energy, thus rendering it invisible to the experiment. Every RR spectra across different pH values and axial ligands are very similar. There is no evidence of significant energy shifts either as an effect of pH or axial ligand mutation, except for the ν2 (364 cm^{-1}) band which presents an upshift of 2 cm^{-1} for the M160Q.

Table S5. Reorganization energies obtained from Arrhenius plots using Laviron's working curve or from Marcus-DoS fits of trumpet plots.

	λ_{Arr}	λ_{MDoS}
WT	0.46	0.45
M160H	0.63	0.7
M160Q	0.45	0.45

Table S6. Electronic coupling decays for the ET reaction from Cytochrome c_{552} to Cu_A from *T. thermophilus*. Calculations were performed applying the *pathways* algorithm (11) to the three possible structures reported by Muresanu *et al*.(12) for the inter-protein complex. Only the five best pathways in terms of electronic coupling are reported in the table. These pathways differ among them only in small details regarding atom types and connectivities involved (*ie*. a through space jump *vs* a hydrogen bond jump) and, therefore, coupling decays are very similar. Note that, for the sake of brevity, each pathway's label consists only of the residues involved, although pathways with identical label may involve different atomistic routes for electron transfer. Other pathways with significantly lower $|H_{DA}|$ values are not reported as they are not relevant to the ET reaction.
Two sets of five pathways are shown or each of the three possible structures of the Cyt c_{552}/Cu_A complex. The first set represents the overall best couplings, while the second set was obtained by considering no covalent bond between S_{Met} and Cu atoms in the pathways calculations. Blue: amino acids belonging to Cyt c_{552}. Red: amino acids belonging to Cu_A.

Cyt c_{552}/Cu_A

Ligands involved	Pathway	Coupling decay
	Structure 1	
All	HEC-ALA87-PHE88-MET160-CUA	5.83040E-05
	HEC-ALA87-PHE88-MET160-CUA	5.43024E-05
	HEC-ALA87-PHE88-MET160-CUA	5.03145E-05
	HEC-ALA87-PHE88-MET160-CUA	4.04523E-05
	HEC-ALA87-PHE88-MET160-CUA	3.49824E-05
Not M160	HEC-ALA87-PHE88-HIS114-CUA	2.71003E-05
	HEC-ALA87- HIS114-CUA	1.91004E-05
	HEC-MET69-VAL68-GLY156-HIS157-CUA	1.74867E-05
	HEC-ALA87-PHE88-HIS114-CUA	1.66781E-05
	HEC-ALA87-PHE88-HIS114-CUA	1.62602E-05
	Structure 2	
All	HEC-MET69-VAL68-MET160-CUA	7.42011E-05
	HEC-ALA87-PHE88-MET160-CUA	5.15771E-05
	HEC-MET69-VAL68-MET160-CUA	4.48470E-05
	HEC-MET69-VAL68-MET160-CUA	3.58197E-05
	HEC-MET69-VAL68-MET160-CUA	3.51613E-05
Not M160	HEC-ALA87-PHE88-HIS114-CUA	2.25502E-05
	HEC-ALA87-PHE88-HIS114-CUA	1.82601E-05
	HEC-ALA87-PHE88-HIS114-CUA	1.81015E-05
	HEC-ALA87-PHE88-HIS114-CUA	1.38918E-05
	HEC-MET69-SER70-PHE88-HIS114-CUA	1.38869E-05
	Structure 3	
All	HEC-MET69-VAL68-MET160-CUA	3.45105E-05
	HEC-MET69-VAL68-MET160-CUA	2.63216E-05
	HEC-MET69-VAL68-MET160-CUA	1.94847E-05
	HEC-MET69-VAL68-MET160-CUA	1.86437E-05
	HEC-MET69-VAL68-MET160-CUA	1.64420E-05
	HEC-ALA87-PHE88-HIS114-CUA	1.24082E-05

	HEC-ALA87-PHE88-HIS114-CUA	1.19843E-05
Not M160	HEC-MET69-VAL68-GLY156-HIS157-CUA	9.83603E-06
	HEC-ALA87-PHE88-HIS114-CUA	8.72567E-06
	HEC-ALA87-PHE88-HIS114-CUA	8.28323E-06

Table S7. Electronic coupling decays for ET from Cu_A to heme *b* in *T. thermophilus'* COX ba_3calculated with the *pathways* algorithm. For each structure two sets of five pathways are shown. The first set represents the overall best couplings, while the second set was obtained by doing pathways calculations considering no covalent bond between N_{His157} and Cu atoms. For the sake of brevity, each pathway's label consists only of the residues involved. One should note, however, that each pathway differs in its composition, regarding both atom types and the connectivities involved (*ie*. a through space jump *vs* a hydrogen bond jump). Thus, pathways with identical label may involve different atomistic routes for electron transfer. Many of these differences are subtle having and so are expected to exert a small impact on $|H_{DA}|$.

Cytochrome ba_3

Ligands involved	Pathway	Coupling decay
All	CUA-HIS157-ARG450-HEM	2.30214E-05
	CUA-HIS157-ARG450-HEM	1.76994E-05
	CUA-HIS157-ARG450-HEM	1.64145E-05
	CUA-HIS157-ARG450-HEM	1.61133E-05
	CUA-HIS157-ARG450-HEM	1.55078E-05
Not His157	CUA-GLN151-TYR152-ARG450-HEM	1.25082E-05
	CUA-GLN151-TYR152-ARG450-HEM	1.11181E-05
	CUA-GLN151-TYR152-ARG450-HEM	7.75998E-06
	CUA-GLN151-TYR152-ARG450-HEM	7.50492E-06
	CUA-GLN151-TYR152-ARG450-HEM	6.77235E-06

Table S8. Atomic contributions to the HOMO wavefunction, which define the covalency.

	$Cu^{1.5}$- $Cu^{1.5}$		Cu^{1}- Cu^{1}	
	σ_u^*	π_u	σ_u^*	π_u
S_{Cys153}	0.23	0.13	0.13	0.12
S_{Cys149}	0.22	0.11	0.16	0.21
N_{His114}	0.00	0.01	0.01	0.00
N_{His157}	0.00	0.02	0.02	0.01
O_{Gln151}	0.00	0.01	0.01	0.00
S_{Met160}	0.01	0.11	0.02	0.01

References

1. George GN, Pickering IJ (1995) EXAFSPAK: A suite of computer programs for analysis of X-ray absorption spectra. *SSRL, Stanford.*

2. Blackburn NJ, Ralle M, Gomez E, Hill MG, Pastuszyn A *et al.* (1999) Selenomethionine-substituted *Thermus thermophilus* cytochrome ba_3:

Characterization of the Cu_A site by Se and Cu K-EXAFS. *Biochemistry* 38:7075-7084.

3. Siluvai GS, Mayfield M, Nilges MJ, DeBeer George S, Blackburn NJ (2010) Anatomy of a red copper center: spectroscopic identification and reactivity of the copper centers of Bacillus subtilis Sco and its Cys-to-Ala variants. *J. Am. Chem. Soc.* 132:5215-5226.

4. Case DA, Darden TA, Cheatham III TE, Simmerling CL, Wang J *et al.* (2010) AMBER 11. *University of California, San Francisco*.

5. Marti MA, Capece L, Bidon-Chanal A, Crespo A, Guallar V *et al.* (2008) Nitric oxide reactivity with globins as investigated through computer simulation. *Meth. Enzymol.* 437:477-498.

6. Dupradeau FY, Pigache A, Zaffran T, Savineau C, Lelong R *et al.* (2010) The RED tools: advances in RESP and ESP charge derivation and force field library building. *Phys. Chem. Chem. Phys.* 12:7821-7839.

7. Izquierdo J, Vega A, Balbás LC, Sánchez-Portal D, Junquera J *et al.* (2000) Systematic ab initio study of the electronic and magnetic properties of different pure and mixed iron systems. *Phys. Rev. B* 61:13639.

8. Crespo A, Scherlis DA, Martí MA, Ordejón P, Roitberg AE *et al.* (2003) A DFT-based QM-MM approach designed for the treatment of large molecular systems: Application to chorismate mutase. *J. Phys. Chem. B* 107:13728-13736.

9. Perdew JP, Burke K, Ernzerhof M (1996) Generalized gradient approximation made simple. *Phys. Rev. Lett.* 77:3865-3868.

10. Frisch MJ, Trucks GW, Schlegel HB, Scuseria GE, Robb MA *et al.* (2009) Gaussian 09, revision A. 02; Gaussian. *Inc : Wallingford, CT*.

11. Beratan DN, Betts JN, Onuchic JN (1991) Protein electron transfer rates set by the bridging secondary and tertiary structure. *Science* 252:1285.

12. Muresanu L, Pristovsek P, Löhr F, Maneg O, Mukrasch MD *et al.* (2006) The Electron Transfer Complex between Cytochrome c_{552} and the Cu_A Domain of the *Thermus thermophilus* ba_3 Oxidase. *J. Biol. Chem.* 281:14503.

13. Hunsicker-Wang LM, Pacoma RL, Chen Y, Fee JA, Stout CD (2005) A novel cryoprotection scheme for enhancing the diffraction of crystals of recombinant cytochrome ba_3 oxidase from *Thermus thermophilus*. *Acta Crystallogr. D* 61:340-343.

14. Abriata LA, Ledesma GN, Pierattelli R, Vila AJ (2009) Electronic Structure of the Ground and Excited States of the Cu_A Site by NMR Spectroscopy. *J. Am. Chem. Soc.* 131:1939-1946.